Dual-rail encoding with superconducting cavities

James D. Teoh[a,b,c,1] , Patrick Winkel[a,b,c,1] , Harshvardhan K. Babla[a,b,c], Benjamin J. Chapman[a,b,c] , Jahan Claes[a,b,c] , Stijn J. de Graaf[a,b,c] ,
John W. O. Garmon[a,b,c], William D. Kalfus[a,b,c], Yao Lu[a,b,c], Aniket Maiti[a,b,c], Kaavya Sahay[a,b,c] , Neel Thakur[a,b,c] , Takahiro Tsunoda[a,b,c],
Sophia H. Xue[a,b,c] , Luigi Frunzio[a,b,c] , Steven M. Girvin[a,b,c] , Shruti Puri[a,b,c], and Robert J. Schoelkopf[a,b,c,1]

The design of quantum hardware that reduces and mitigates errors is essential for practical quantum error correction (QEC) and useful quantum computation. To this end, we introduce the circuit-Quantum Electrodynamics (QED) dual-rail qubit in which our physical qubit is encoded in the single-photon subspace, $\{|01\rangle, |10\rangle\}$, of two superconducting microwave cavities. The dominant photon loss errors can be detected and converted into erasure errors, which are in general much easier to correct. In contrast to linear optics, a circuit-QED implementation of the dual-rail code offers unique capabilities. Using just one additional transmon ancilla per dual-rail qubit, we describe how to perform a gate-based set of universal operations that includes state preparation, logical readout, and parametrizable single and two-qubit gates. Moreover, first-order hardware errors in the cavities and the transmon can be detected and converted to erasure errors in all operations, leaving background Pauli errors that are orders of magnitude smaller. Hence, the dual-rail cavity qubit exhibits a favorable hierachy of error rates and is expected to perform well below the relevant QEC thresholds with today's coherence times.

quantum computing | superconducting circuits | quantum information | quantum error correction

There has been remarkable progress in the physical implementation of quantum information processing devices over the past two decades. Several platforms, including trapped ions (1–5), neutral atoms (6–9), and superconducting circuits (10, 11), have advanced to the stage where systems with dozens or hundreds of physical qubits can be assembled and programmed (12, 13) to perform simple algorithms. But even for the so-called Noisy Intermediate Scale Quantum (NISQ) applications (14) that are being investigated today, significant improvements are necessary in the error rates for all types of operations, including initialization and measurement as well as single and two-qubit quantum gates. Moving beyond the current NISQ era will require the implementation of quantum error correction that performs well enough to realize significant gains in logical fidelity. While some of the performance levels of physical qubits are now approaching the theoretical thresholds that are required (15), when and how practical error correction might be achieved remains an outstanding question.

Quantum error correction (QEC) is challenging because of many simultaneous requirements. These include a significant overhead in the number of physical qubits used to encode logical information, the rapid operation of a complex sequence of gates and measurements to detect errors, and the high fidelity and precision of the components and operations that make up the system. Finding more efficient schemes for QEC that can ease these requirements is a very active area of current research. A wide range of approaches has been explored, including more efficient codes (16), qubits that have structure or bias (17–23) in their noise processes and the modifications of encoding schemes to utilize this structure (24–30), code switching or "pieceable" constructions (31, 32) that do not require fully transversal operations, and correction schemes that can flag (33, 34) certain errors. One can even build redundancy into a single physical system, replacing the usual qubits with multilevel systems such as qutrits (35). Bosonic encodings (36) such as the GKP code (37–41), cat codes (17, 42–45), or binomial codes (46–49) have proven to be especially hardware efficient.

When choosing an error correction architecture, it is important to remember that there is a natural hierarchy of physical and logical errors. Not all errors occur with equal probability nor are they equally harmful to the code. On the logical level, detected erasure errors are especially benign, having both significantly higher thresholds and more favorable scaling with code distance (50–54). The most studied error model—Pauli errors, the most well-studied error model, are also correctable but have lower thresholds and a less favorable scaling with code distance. Finally, the accumulation of undetected leakage errors out of the code space is an uncorrectable error

Significance

Here, we propose an architecture for quantum computing that applies the dual-rail encoding from quantum optics to a superconducting quantum circuit platform. In doing so, we not only benefit from the error detection properties of this encoding but also exploit the strong nonlinearities available in superconducting circuits, which enable gate-based quantum computation. While any useful quantum computer is expected to need quantum error correction, direct error detection allows us to know exactly where and when a qubit has an error, making error correction much easier. By designing the dual-rail qubits such that most of their errors can be detected, we believe that practical quantum error correction can already be achieved with the coherence times of today's superconducting circuits.

and therefore most damaging (55–62). Aligning the physical behavior of gates and qubits to respect this hierarchy is therefore another important strategy for efficient QEC. Erasures are the dominant errors for some platforms such as linear quantum optics (63–65). An important recent insight (66) is that one may also choose or design physical qubits and operations where additional measurements can detect certain errors and then allow them to be converted to erasures, easing the thresholds and overhead requirements for QEC.

Superconducting microwave cavities are attractive candidates for hardware-efficient error correction. Microwave resonators can be implemented in planar or 3D geometries and typically have longer lifetimes (67–70) than nonlinear qubits containing Josephson junctions. Moreover, they exhibit little or no intrinsic dephasing (40, 70–72), with the predominant error mechanism simply being photon loss. This means that they naturally have a type of bias in their decoherence. Over the last few years, these properties have allowed experiments that demonstrate quantum memories (36, 40, 45), single-qubit quantum gates (73, 74), and remote entanglement (75) where the error correction approaches or even exceeds the breakeven point and logical fidelity begins to improve. Just as qubit-based codes incur an overhead because they require multiple physical qubits per logical qubit and additional measurement ancillae, bosonic codes do incur an increase in the decay rate proportional to the number of photons stored in the system. In addition, transmons or other traditional superconducting qubits are still required to enable the nonlinear operations necessary for control and measurement in the codespace. These ancillae then introduce additional error channels that can limit fidelity unless they can be managed and prevented from propagating to the bosonic logical qubit (18, 71, 74).

Here, we propose a platform for bosonic error correction by combining the previously developed techniques of circuit QED and an implementation of the dual-rail encoding with a single photon stored in a pair of coupled microwave cavities. Employing microwave cavities for the dual-rail encoding uses a small number of photons and preserves the noise bias, where photon loss only appears as a detectable erasure. We argue that this system can have a remarkable and highly favorable hierarchy of error rates, with Pauli errors that are orders of magnitude weaker than erasures, and leakage that is even smaller. In addition, we describe a complete set of one- and two-qubit operations that use a beamsplitter interaction between the cavities and a dispersively coupled transmon ancilla to enable high-fidelity preparation, measurement, and nonlinear control. We show how the dominant physical errors, including decay, heating, and dephasing in the transmon ancilla, can be effectively detected and converted to erasures, with only second-order contributions to a residual rate of Pauli errors. Even with current levels of decoherence and previously demonstrated operation speeds (76, 77), this scheme will allow postselected algorithms with fidelity significantly beyond that of today's NISQ machines. Finally, this approach should perform well in concatenated QEC schemes such as the surface code (25, 66, 78–80), enabling a faster path to fault-tolerant quantum computing.

1. Results

A. Dual-Rail Cavity Qubit. The concept of the superconducting dual-rail cavity qubit is based on the intrinsic noise bias of superconducting cavities, for which single-photon loss is the dominant physical error channel and the pure dephasing caused by fluctuations in cavity frequency is orders of magnitude smaller, at least for an isolated cavity. Furthermore, the single-photon loss rates for superconducting cavities are among the smallest error rates measured in any superconducting device (81) and are likely to improve at least as rapidly as qubits based on Josephson junctions with continuing advances in material science and fabrication.

The dual-rail superconducting qubit we present here has a similar encoding to that used in linear quantum optics platforms (82), where logical information is encoded in two distinguishable bosonic modes, but with access to a set of quantum nondemolition (QND) measurements and nonlinear controls afforded by the circuit quantum electrodynamics (cQED) (11, 119) toolkit. Crucially, we can use the nonlinearity of a transmon (or other) ancilla to directly perform two-qubit entangling gates and also QND measurements such as joint photon-number parity measurements on two cavities. These capabilities mean, in contrast to other implementations, we can realize a gate-based approach for the dual-rail qubit with no need for heralding, with the ability to detect many types of physical errors at the hardware level.

A version of dual-rail encoding entirely based on transmon qubits was recently suggested (29). Unlike microwave cavities, transmons have little inherent noise bias, with dephasing rates often comparable to their decay rates. While we could detect decay events in this transmon dual-rail qubit, dephasing will remain the dominant error source, introducing both Pauli X and Z errors. In a recent implementation (83) the desired noise bias was engineered by tuning two transmons on resonance with each other.

Instead of two propagating optical modes, we choose the two rails to be superconducting standing-wave cavity modes with distinct microwave frequencies. These could be two modes of the same resonator (84), but here, we will discuss the case where they are in separate but adjacent resonators, as shown in Fig. 1. The logical codewords are $|0\rangle_L = |01\rangle$ and $|1\rangle_L = |10\rangle$. By encoding the logical state of the qubit in the single-photon subspace of the joint cavity Hilbert space with odd joint photon-number parity, we are able to convert the dominant errors in the cavity system, namely single-photon loss to the common ground state $|00\rangle$, into detectable erasure errors by means of joint-parity measurements. In addition, photon gain events in the cavities, which are generally rare in thermal equilibrium, are also detectable by the same measurement, leaving cavity dephasing as the dominant Pauli error in the system. The error probability and scaling during idling time are summarized in Table 1. This shows a remarkable physical error hierarchy that follows the optimal structure for quantum error correction codes that include erasure conversion. In following sections, we will see that Pauli errors remain small even when we introduce the transmon ancilla and cavity–cavity coupler needed for a full set of operations.

Compared to other bosonic codes (37, 46, 85), there is little increase in the photon number when using the dual-rail encoding relative to the simple "single-rail," or Fock $\{|0\rangle, |1\rangle\}$ encoding. The main cost is we now need two cavity modes per qubit instead of one, and we double the number of photons (from $\bar{n} = 0.5$ to $\bar{n} = 1$). Single-qubit gates for Fock $\{|0\rangle, |1\rangle\}$ cavity qubits are more difficult and slower, requiring extensive use of a transmon ancilla (73). In a dual-rail cavity qubit, arbitrary single-qubit rotations are achieved with a simple switchable beamsplitter interaction between the cavities, by pumping a dedicated nonlinear coupler (76, 77). This is another vast simplification compared to other bosonic encodings.
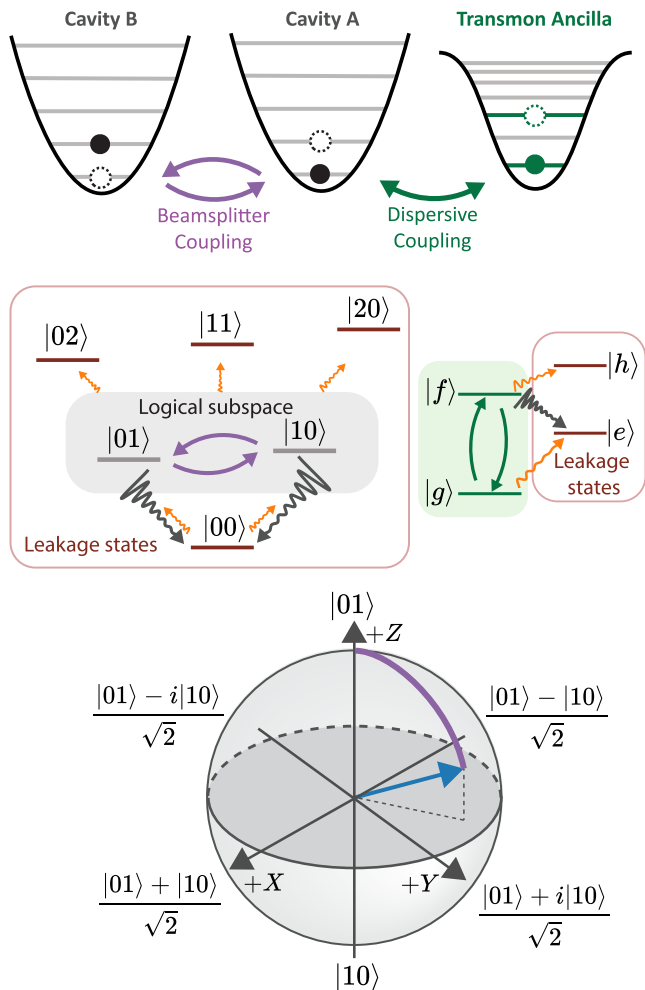
Fig. 1. The cavity dual-rail qubit is composed of two standing superconducting cavities taking the role of the two waveguide modes in linear quantum optics. The cavities are coupled by a switchable beamsplitter interaction. The logical code words are encoded in the single-photon subspace of the cavity system, with $|0\rangle_L = |01\rangle$ and $|1\rangle_L = |10\rangle$, for which the beamsplitter interaction is sufficient to facilitate arbitrary single-qubit rotations. Energy relaxation events into the common ground state $|00\rangle$ as well as single heating events into the higher energy states $|11\rangle$, $|20\rangle$, and $|02\rangle$ bring the system into a leakage space distinguished from the logical subspace by the joint photon-number parity. Therefore, the dominant error in the cavity system, single-photon decay, can be converted into erasure errors by measuring the joint-parity. A single transmon ancilla is dispersively coupled to one of the cavities and acts as a resource for non-Gaussian operations. By operating the transmon in the g-f-manifold, we are able to detect decay events in the ancilla, expected to be the most dominant error in the system for state-of-the-art realizations, and convert them into erasure errors as well.

Since the (frequency-converting) beamsplitter interaction is activated using parametric processes, the cavities are not on resonance during the idling time, resulting in a large on–off ratio. The amplitude and phase of the beamsplitter pumps are analogous to the usual RF drives used to control transmon qubits, enabling techniques such as dynamical decoupling (86, 87) to further suppress dephasing errors as well as unwanted effects such as no-jump backaction arising from differences in cavity single-photon decay rates (*SI Appendix,* Section D).

Non-Gaussian operations on the dual-rail cavity qubit use the transmon ancilla as the source of nonlinearity. This includes state preparation, logical readout, QND cavity loss (joint-parity) detection, and the two-qubit entangling gates. Since transmon errors occur more frequently than all cavity idling errors, we design protocols to preserve the error hierarchy that exists for

idle dual-rail qubits by detecting first-order transmon errors after the sequence.

B. State Preparation and Measurement. We now describe how to perform preparation and readout of logical states on a dual-rail qubit, which may also be constructed to avoid first-order sensitivity to most physical errors. The general approach is to use the dispersive interaction between one of the cavities and the ancilla transmon to learn logical state information from repeated photon-number parity measurements. We may then majority vote on many rounds of measurement outcomes to reach high assignment fidelity (89) by using the most common outcome to decide the overall measurement result. This exponentially suppresses the effects of transmon errors and transmon readout errors at the cost of a small increase in the ongoing erasure rate due to cavity photon loss. For the proposed measurement scheme, logical readout fidelity for a dual-rail qubit is expected to be better than any other known qubit platform.

The QND nature of parity measurements performed on single cavities (90) means we can also use them to verify logical state preparation to very high fidelity. Preparing a state in the logical Z basis is simply a matter of loading a single photon into one of the two cavities. This may be done via optimal control pulses (73) or cavity-transmon sideband drives (89, 91–93) and then verified with subsequent parity measurements to achieve error-robust state preparation with success probability $> 99\%$. Unsuccessful state preparation may be treated as an erased qubit, or we can allow for multiple attempts at state preparation to boost the success probability. Due to low idling error rates of the dual-rail (Table. 1), the additional measurement time need not introduce logical errors at a substantial rate. Once again, the dominant errors are detectable leakage errors, i.e., erasures.

For logical readout of a dual-rail qubit, we must ascertain whether a photon is in cavity Alice, $|0\rangle_L$, or Bob, $|1\rangle_L$, or in the case of a leakage event due to photon loss, neither cavity. One simple way to do this is to measure the photon number parity in both cavities sequentially using the g-e-manifold of the transmon ancilla (43, 90), which requires a time $\sim 1/\chi_{\mathrm{ge}} \sim 0.1 - 1\,\mu\mathrm{s}$ and is shown in Fig. 2. We may measure the parity sequentially using the same ancilla and swapping the cavity states in between each parity measurement, or an additional ancilla transmon for the second cavity can be added to the architecture if desired. If we are in the logical $|0\rangle_L$ state, we should obtain the transmon measurement string (e_a, g_b) since we read out state $|e\rangle$ when there are an odd number of photons in the cavity. In the case of prior photon loss, we obtain (g_a, g_b) and flag the measurement as an erasure.

The probability of mistaking $|0\rangle_L$ for $|1\rangle_L$ (and vice versa) should be exceedingly small even in the presence of decoherence. First-order errors in the transmon and cavities give measurement outcomes (g_a, g_b) and (e_a, e_b), which we flag as additional erasure errors. A combination of at least two errors is necessary for logical misassignment, a probability we estimate to be below 10^{-4} for realistic coherence times and transmon readout fidelities (94, 95).

Dephasing on the cavity is not an issue when preparing and measuring dual-rail qubits in the Z basis, so we may operate the transmon ancilla in the g-e-manifold without the need to flag transmon errors. Even though transmon decay can corrupt an individual parity measurement outcome, we may still correctly measure logical information via subsequent parity measurements to increase readout fidelity. Alternatively, we can map information about the cavity states onto the transmon using photon-number selective π pulses. In combination with shelving the transmon excitation into higher states, we expect to

Table 1. The dual-rail cavity qubit is composed of multiple hardware components—two superconducting cavities, a single parametric coupler, and a single transmon ancilla, as shown in Fig. 1

Error process	Scaling	Probability in 1 µs	Noise bias	Effective lifetime	Error type	Detection
Cavity photon loss	$\bar{\kappa}t$	10^{-3}	1	1 ms	Erasure	JP
Cavity heating	$\bar{n}_{th}\bar{\kappa}t$	10^{-5}	10^2	100 ms	Erasure	JP
Cavity dephasing	$\gamma_{\varphi}t$	10^{-4}	10^1	10 ms	Phase flip	-
Ancilla heating	$\bar{n}_{th,A}\Gamma_{1,A}t$	10^{-4}	10^1	10 ms	Phase flip	M
No-jump backaction	$\left(\frac{1}{4}\Delta\kappa t\right)^2$	10^{-6}	10^3	1 s	Phase flip	-
Cavity photon loss + heating	$\bar{n}_{th}\left(\bar{\kappa}t\right)^2$	10^{-8}	10^5	100 s	Bit flip	-
Cavity heating $\times 2$	$3\left(\bar{n}_{th}\bar{\kappa}t\right)^2$	10^{-9}	10^6	~ 1 h	Leakage	JSP

To estimate the physical error rate of the proposed dual-rail qubit during idling time, and the logical errors in the encoded qubit they can cause, we assume typical performances achievable for the individual components today. By construction, the hierarchy of these events, i.e., their probability of occurrence, aligns with the desired scaling for an outer QEC layer: The dominant error is photon loss out of the computational space caused by cavity relaxation at rate $\bar{\kappa} = (\kappa_a + \kappa_b)/2$, which, by measuring the joint-parity (JP), can be converted into erasure errors. As a consequence, erasure errors, though still rare, are significantly more likely than Pauli errors. During the idling time, phase flip events are predominantly caused by dephasing events in the cavity system or heating events in the transmon, where $\bar{n}_{th,A}$ is the average thermal ancilla population and $\Gamma_{1,A}$ the energy relaxation rate. By measuring the transmon (M) and ensuring that it remains in its ground state, we can detect ancilla heating events, at least to first order. No-jump backaction arises when there is a finite difference between the single-photon decay rates of the cavities given by $\Delta\kappa = \kappa_b - \kappa_a$. Over time, the weighting of a dual-rail qubit superposition changes to increase the probability of the photon being in the longer-lived cavity, despite no photon loss being detected. This is a second-order effect and is a type of phase flip type error. Unlike cavity dephasing, this error can change the qubit's populations. The closest error that resembles a bit flip error is the unlikely combination of a cavity decay and heating event, resulting in an indirect transition between the logical codewords at extremely low rates. Leakage events undetectable by the joint-parity measurement are extremely rare, as they require two heating events in the cavities to bring the dual-rail qubit into a state with odd joint-parity outside the logical codespace. However, these events could still be detected with a QND measurement(88) of the joint "superparity," (JSP) as they have a different value for $(n_a + n_b) \bmod 4$. For the calculation of the error probabilities, we assume single-photon decay rates of $\kappa_a = (1.5\,\text{ms})^{-1}$ and $\kappa_b = (0.5\,\text{ms})^{-1}$ for the cavities, $\Gamma_{1,A} = (100\,\mu\text{s})^{-1}$ for the ancilla transmon, pure dephasing rates $\gamma_{\varphi,a} = \gamma_{\varphi,b} = (20\,\text{ms})^{-1}$, and a thermal population $\bar{n}_{th} = \bar{n}_{th,A} = 0.01$ for all quantum elements. The noise bias of the dual-rail specifically refers to erasure errors happening much more frequently than all other types of errors such as Pauli and leakage errors. The noise bias is quantified for each error process by comparing to the cavity photon loss error rate, the dominant source of erasure errors in the system when idling.

achieve high logical readout fidelities even with a single round of measurements (89).

By repeating each round of parity measurements three times, we can majority vote on the outcomes to further suppress the effects of transmon errors. Practically, this means fewer unnecessary erasure flags due to transmon errors along with a small increase in erasure flags due to cavity photon loss. We also note that majority voting suppresses the infidelity of the transmon measurements themselves. Here, we consider the consequence of two types of measurement errors: a misassignment of the transmon state due to the finite SNR of the measurement and transmon decay during readout. In both cases, the inferred

transmon state does not coincide with the physical state, which can corrupt the subsequent measurement outcome after resetting into the ground state (96). Alternatively, we can use an unconditional reset (97) or no reset at all and instead update the expected measurement outcomes. A quantitative comparison of two particular measurement strategies is shown in Fig. 2, assuming state-of-the-art experimental hardware.

In general, the optimal measurement strategy is highly context and device dependent, with tradeoffs between total measurement time, additional erasure rate, and measurement fidelity. Measurement of ancilla dual-rail qubits in a surface code may prioritize measurement speed over assignment fidelity, whereas postselected
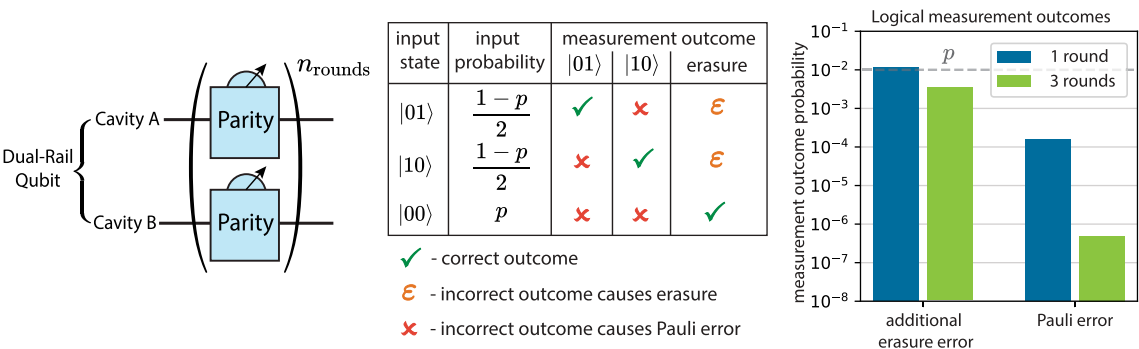

Fig. 2. The logical state of the dual-rail cavity qubit can be extracted from local parity measurements of the individual cavities. The table shows the three most likely input states $|01\rangle$, $|10\rangle$, and $|00\rangle$ together with their input probability, where p is the probability of a photon loss event prior to the measurement, leaving the system in $|00\rangle$. We set $p = 1\%$, which is the erasure probability due to photon loss in the cavities after approximately ten two-qubit gates. Depending on the input state, the outcome of the measurement is either correctly assigned to the actual input state (green ticks), incorrectly flagged as an erasure (orange), or incorrectly assigned to the logical states (red cross) resulting in a Pauli error. By repeating the measurement protocol n times, the measurement errors can be significantly reduced, as shown in the *Right* panel. For a single round of measurements (blue bars), ancilla readout errors are mainly converted into false-positive erasure errors. With three rounds of measurements and majority voting (*SI Appendix*, Section B), we become much more robust to transmon errors, leading to a factor of five reduction in the additional erasures and orders of magnitude reduction in the logical assignment error. As we increase the number of measurement rounds even further, the total measurement time gets longer, and so the probability of cavity photon loss increases, eventually increasing the chance of erasure again (not shown). Hence, due to finite transmon coherence times and readout fidelities, there can be improvement in measurement performance when using 3 rounds instead of 1 round. The simulation models transmon decay during readout and other measurement errors (*SI Appendix*, Section A). We set $T_1^{ge} = 100\,\mu\text{s}$, $T_\varphi^{ee} = 100\,\mu\text{s}$, and $\kappa_a = \kappa_b = (1\,\text{ms})^{-1}$.

short-depth circuits may favor assignment fidelity above all else. More measurement strategies are discussed in *SI Appendix, Section B*. The examples in Fig. 2 show the minimum needed to suppress transmon errors and the benefits from majority voting. An experimental implementation of the state preparation and logical readout of a dual-rail cavity qubit has been recently reported in ref. 98, demonstrating a logical misassignment error of $(1.7 \pm 0.3) \times 10^{-4}$ for a single round and $(3 \pm 1) \times 10^{-5}$ for two rounds of measurement.

C. Single-Qubit Rotations.

Single-qubit gates in the dual-rail subspace are realized by a simple beamsplitter interaction between the cavities using a dedicated coupling element (76, 77). The combination of beamsplitter strength and duration, which are controlled by microwave pump signals in an experiment, define the polar angle of the rotation, while arbitrary rotations around the Z-axis can be implemented in software by changing the phase of the pump(s). This parametrizable control is in many ways analogous to typical use of RF signals for transmon single-qubit gates. A SWAP gate between the cavities is equivalent to a π-pulse, and a 50–50 beamsplitter corresponds to a $\pi/2$-pulse. Changing the pump phase changes the equator axis we rotate around on the Bloch sphere. Techniques for suppressing control errors, such as composite pulses, can be directly transferred to our beamsplitter control (99, 100). Moreover, we can also make use of dynamical decoupling (86, 87) to further enhance the dephasing time of our dual-rail qubit.

High-speed beamsplitters (77) and randomized benchmarking (76) of single-qubit gates in the dual-rail subspace have recently been experimentally demonstrated that approach 99.98% gate fidelity when combined with an erasure check, in times of ~50–100 ns per gate. This is on par with single-qubit gates in transmons (101). Unlike a transmon qubit, there is no inherent speed limit set by the finite anharmonicity of the energy spectrum (102, 103), which increases leakage out of the computational space as we decrease gate times. It is also observed that the beamsplitter interaction does not induce any additional leakage errors out of the dual-rail subspace, aside from the expected (and detectable) decay to the $|00\rangle$ state set by the bare cavity single-photon decay rates.

Using a parametric beamsplitter coupler allows our cavity modes to have large detunings, with vanishingly small swapping rates between the cavities in the absence of the pumps. Moreover, any static coupling between the cavities (within or between dual-rail qubits) simply leads to a renormalization of the cavity frequencies via mode hybridization, and is automatically compensated by calibrating to the dressed values that are observed in an experiment.

The ease of arbitrary single-qubit rotations in the dual-rail encoding is a huge advantage compared to other error-correctable bosonic codes such as GKP (37), Binomial (46), or 4-legged cats (17, 42). While universal control of a harmonic oscillator via a transmon ancilla has been shown in many frameworks (72, 73, 104), these approaches are comparatively slow to execute, require numerical optimization, and, most importantly, are highly susceptible to ancilla transmon errors.

D. Erasure Conversion.

A keystone of the proposed dual-rail scheme is that we can perform QND detection of leakage out of the logical subspace caused by loss or gain of a photon in the cavities. For QEC protocols, the knowledge about the exact location of the error enables us to convert these otherwise pernicious leakage events into erasure errors, which are much easier to correct than Pauli errors. Therefore, we refer to this leakage detection scheme as the erasure check.

Our erasure check is based on measuring the joint photon-number parity of the two cavities in a single dual-rail qubit. The dual-rail subspace has odd joint-parity but gain or loss of a photon changes this to even. Hence, QND joint-parity measurements allow us to perform erasure checks without destroying the logical states. Our specific scheme for measuring joint-parity is an extension of the well-established parity measurement scheme for an individual cavity (43, 90) and relies on the dispersive interaction to a single transmon ancilla as shown in Fig. 3.
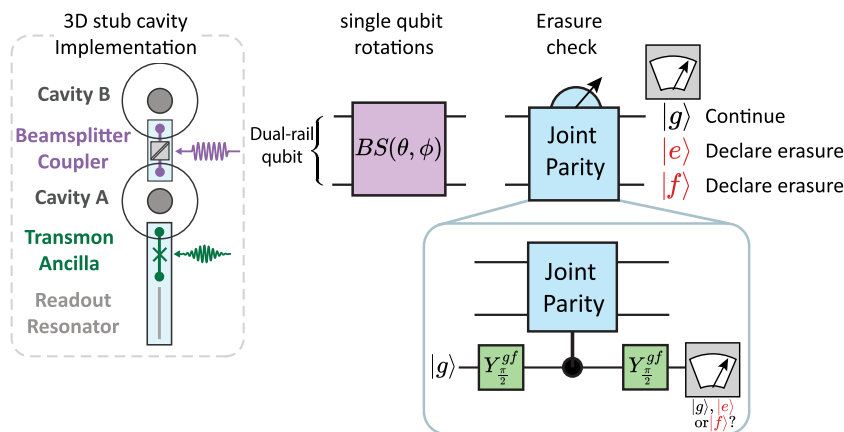

Fig. 3. An example of hardware to implement one dual-rail cavity qubit (Fig. 1), shown here as 3D stub cavities, which have already demonstrated (68) single-photon decay times beyond 1 ms, even in the presence of additional nonlinear modes, and have intrinsically low pure dephasing rates reaching at least tens of milliseconds (40, 71, 72). The beamsplitter interaction between the cavities, which is sufficient to implement arbitrary single-qubit rotations in the dual-rail subspace, can be realized with one of several choices of parametrically driven three-wave or four-wave mixing elements (violet), as recently demonstrated in refs. 76 and 77, respectively, without degrading the intrinsic coherence of the cavities. For the non-Gaussian operation, a transmon ancilla is capacitively coupled to one of the stub cavities and is operated in the g-f-manifold to allow for ancilla decay detection with a dedicated readout resonator. A key ingredient for the operation of the dual-rail qubit is the detection of physical errors in the quantum hardware, allowing us to convert leakage events into erasure errors. Such an erasure check is implemented by mapping the joint photon-number parity on the state of the ancilla. The ancilla starting in the ground state $|g\rangle$ is initialized in the $|+X\rangle$ state with a $\pi/2$ pulse. While photon-number parity measurements in a single cavity have been already demonstrated, we can measure the joint-parity by activating the beamsplitter interaction between the cavities at the same time. The second $\pi/2$ pulse maps the odd joint-parity states on the ground state $|g\rangle$ of the ancilla and the even states on $|f\rangle$. A decay of the ancilla during the operation is flagged by the final state $|e\rangle$. More details on the implementation of these composite operations are found in ref. 88.

Remarkably, by combining a beamsplitter interaction between the two dual-rail cavities with manipulations of a transmon coupled to only one cavity, there are simple procedures (88) for measuring joint properties of the dual-rail qubit, without requiring precise matching of fabrication parameters. For the joint-parity erasure check, we perform a Ramsey sequence on the transmon with a wait time $T = 2\pi/\chi_{gf}$ between the transmon $\pi/2$ pulses. During this time, the dispersive interaction between the transmon and one of the cavities maps photon-number information to the ancilla state, which is then measured at the end of the sequence. By also activating a beamsplitter interaction during the wait time, excitations swap back and forth between the cavities, allowing the ancilla to measure properties of both cavity states.

We find that for a particular beamsplitter strength $g_{bs} = \sqrt{3}\chi_{gf}/2$ and detuning $\Delta = \chi_{gf}/2$ from resonance, we measure the joint-parity information of both cavities, which return to their initial states at the end of the sequence (up to a deterministic cavity phase shift that is easily tracked in software). In experiment, matching these conditions is easily achieved by adjusting the amplitude and detuning of microwave drives applied to the parametric coupler. These conditions are derived in *SI Appendix, Section E* and explored further in Tsunoda et al. (88). In contrast to the joint-parity measurement implemented in ref. 105, our method allows us to reserve the $|e\rangle$ level to detect transmon decay events and only requires the ancilla to be coupled to one cavity.

The purpose of the erasure check is to convert cavity leakage errors to erasure errors. However, the erasure check itself is error prone. Of particular concern are transmon decay errors that happen with probability $\sim 10^{-2}$ during the check. Left undetected, these errors induce cavity dephasing—equivalent to a logical Pauli error on our dual-rail qubit. To combat this, we operate the transmon in the g-f-manifold and perform three-state readout (89, 106–109, 118, 120, 122) that distinguishes among the states $|g\rangle$, $|e\rangle$ and $|f\rangle$. Measuring $|e\rangle$ now flags transmon decay

events which are also converted to qubit erasures. Measuring $|f\rangle$ signals that we have leaked out of the dual-rail subspace.

With this modification, the cost associated with each erasure check is an additional erasure probability on the $\sim 10^{-2}$ level and additional Pauli errors on the $\sim 10^{-4}$ level, due to second-order errors in the transmon. Since the construction of the erasure check is transparent to transmon dephasing (110), we also see that transmon dephasing errors increase the erasure probability at the $\sim 10^{-2}$ level (Table 2) by randomizing the even/odd measurement outcomes, hence representing a false-positive leakage detection event. When a qubit passes the erasure check despite being in a leakage state, we suffer from a false negative leakage detection event similar to a dark count in quantum optics. These errors will go on to cause Pauli errors in subsequent gate operations until they are most likely detected in the next round of leakage detection. These errors are still effectively second-order since they require both photon loss and a failed erasure conversion in-between rounds.

E. Two-Qubit Gates. Next, we describe how entangling gates between dual-rail qubits can be constructed so that both cavity and transmon errors can also be detected and converted to erasures.

The key insight is that one needs access to only a single cavity of a dual-rail qubit to realize the logical Z operator of the dual-rail. By driving a beamsplitter interaction between a pair of cavities, one from each of the two dual-rail qubits (Fig. 4), a single transmon can effectively act as a control on both dual-rail qubits. Specifically, our proposed two-qubit entangling gate is the $ZZ(\theta)$ gate, which can be written as

$$
\begin{pmatrix}
1 & & & \\
 & e^{i\theta} & & \\
 & & e^{i\theta} & \\
 & & & 1
\end{pmatrix}, \qquad \textbf{[1]}
$$

Table 2. Physical error events in the quantum hardware during the single and two-qubit operations give rise to erasure and Pauli errors in the logical encoding

Error process	Erasure errors		Pauli errors	
Single-photon loss	$\bar{\kappa} T_{\text{gate}}$	10^{-3}	-	-
No-jump backaction	-	-	$\left(\frac{1}{4}\Delta\kappa T_{\text{gate}}\right)^2$	10^{-6}
Cavity dephasing	-	-	$\gamma_\varphi T_{\text{gate}}$	10^{-4}
Ancilla decay	$\Gamma_1^{ef} T_{\text{gate}}$	10^{-2}	$\Gamma_1^{ef}\Gamma_1^{ge} T_{\text{gate}}^2$	10^{-4}
Undetected ancilla decay	-	-	$\eta_{ge}\Gamma_{1,ef} T_{\text{gate}}$	10^{-4}
Ancilla dephasing	$\Gamma_\varphi^{gf} T_{\text{gate}}$	10^{-2}	$\left(\Gamma_\varphi^{gf} T_{\text{gate}}\right)^2$	10^{-4}
Photon loss + ancilla dephasing	-	-	$\bar{\kappa}\Gamma_\varphi^{gf} T_{\text{gate}}^2$	10^{-5}
Undetected ancilla dephasing	-	-	$\eta_{gf}\Gamma_\varphi^{gf} T_{\text{gate}}$	10^{-6}
Measurement infidelity	η_{gf}	10^{-4}	-	-
Photon loss + meas. infid.	-	-	$\eta_{gf}\bar{\kappa} T_{\text{gate}}$	10^{-7}

The probability of such events is determined by their rate of occurrence and the time interval considered, typically the two-qubit gate duration. For the cavity dual-rail qubit, the duration of quantum operations involving the ancilla $T_{\text{gate}} \propto \chi_{gf}^{-1}$ is inversely proportional to the strength of the dispersive interaction between the cavity and the ancilla, and therefore typically on the order of $T_{\text{gate}} \approx 1\,\mu s$. Erasure errors are caused by single-photon loss events in the cavities happening at an average rate $\bar{\kappa}$ in the cavity system as well as decay and dephasing events in the ancilla and the finite measurement infidelity η_{ij} for distinguishing the ancilla states i and j. In general, the measurement infidelities to distinguish different transmon pointer states are not identical (89), which is why we consider two separate infidelities $\eta_{ge} = 10^{-2}$ and $\eta_{gf} = 10^{-4}$. A difference in the single-photon decay rates $\Delta\kappa = \kappa_b - \kappa_a$ causes a no-jump backaction slowly polarizing the dual-rail toward the cavity with the longer lifetime, but, in contrast to the pure dephasing at rate $\gamma_\varphi = \gamma_{\varphi,a} + \gamma_{\varphi,b}$, contributes only to second-order to the Pauli error rate. By construction of the gates, ancilla decay events during the gate cause a backaction on the cavity system, giving rise to bit flip and phase flip errors at approximately similar rates in the case that they are undetected. For the calculation of the error probabilities, we assume $\kappa_a = (0.5\,\text{ms})^{-1}$, $\kappa_b = (1\,\text{ms})^{-1}$, $\gamma_{\varphi,a} = (20\,\text{ms})^{-1}$, $\gamma_{\varphi,b} = (20\,\text{ms})^{-1}$, $\Gamma_1^{ge} = (100\,\mu s)^{-1}$, $\Gamma_1^{ef} = (100\,\mu s)^{-1}$, $\Gamma_\varphi^{gf} = (100\,\mu s)^{-1}$. Notably, because heating events are rare in the cavities and the ancilla, we are not considering them here, but heating is also detected in most cases.
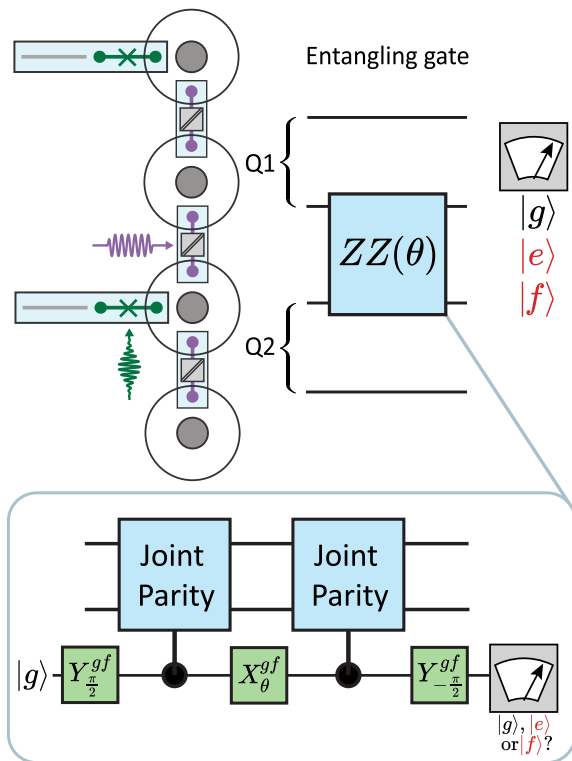
Fig. 4. Hardware implementation of two cavity dual-rail qubits based on 3D superconducting cavities. The two-qubit entangling gate can be realized by a $ZZ(\theta)$ gate performed between the central rails only, for which only one additional coupler is required. For the proposed architecture, the $ZZ(\theta)$ gate can be implemented with the same building blocks as the erasure check and is part of a larger family of error-detectable bosonic gates (88). Crucially for our architecture, transmon errors during the gate are detectable and mapped to flag states ($|e\rangle$: transmon decay, $|f\rangle$: transmon dephasing), allowing for the conversion of these physical errors into erasure errors. With local rotations on the dual-rail qubits, the $ZZ(\theta = \frac{\pi}{2})$ can be transformed into a CNOT or a CZ gate (111, 112).

acting on the two-qubit logical subspace. When $\theta = \pi/2$, this is locally equivalent to a CNOT or CZ gate (111, 112). A $ZZ(\theta)$ gate acting on the subspace $\{|00\rangle, |01\rangle, |10\rangle, |11\rangle\}$ as if each cavity were encoded in the Fock $\{|0\rangle, |1\rangle\}$ code will also realize the $ZZ(\theta)$ for the dual-rail code, provided each of these cavities belongs to a different dual-rail qubit.

Our motivation for the $ZZ(\theta)$ gate implementation is that it can be performed with the exact same hardware required for the erasure checks discussed in the previous section. Though other gate implementations are possible with an ancilla dispersively coupled to both cavities, with this approach, we only need to modify the control pulse sequence (see *SI Appendix*, Section F for derivation).

Similar to the error detection of the erasure check, it is of vital importance to detect transmon errors that happen during the gate in order to preserve the error hierarchy. The construction presented in Fig. 4 ensures that first-order transmon errors are detected when we measure the transmon at the end of the gate, erasing both dual-rail qubits if the transmon is not in $|g\rangle$. Once again, this operation is designed such that Pauli errors are only introduced from second-order hardware errors, when two decoherence events happen during a single gate. The expected error scalings for the $ZZ(\theta)$ gate associated with (detectable) first-order errors and second-order errors are shown in Table 2.

Photon loss during the gate is detectable via separate erasure checks on the two dual-rail qubits after each gate, but

modifications can also be made to the $ZZ(\theta)$ gate pulse sequence to simultaneously perform an erasure check (*SI Appendix*, Section J) in which the transmon can be mapped to the $|f\rangle$ level if one of the input dual-rail qubits was in a leakage state outside the logical subspace. Master equation simulations with various decoherence mechanisms and higher-order nonidealities in the system Hamiltonian are explored in detail in ref. 88 and suggest $\sim 10^{-2}$ erasure probability and $\sim 10^{-4}$ Pauli errors per two-qubit gate, which makes the proposed gate the ideal building block for scalable QEC codes that correct for both Pauli and erasure errors (66).

2. Discussion

A. Reviewing the Error Hierarchy. The principal feature of the proposed dual-rail qubit with superconducting cavities is its strong error hierarchy that persists throughout each operation. The error hierarchy is visualized for feasible coherence times in Fig. 5, ranging from conservative to optimistic hardware performance. Erasure errors result from first-order hardware errors and are predicted to occur with probability $\sim 1\%$ per two-qubit gate. Pauli errors arise to first-order only from cavity dephasing, which is naturally suppressed in superconducting cavities, and from second-order hardware errors that are similarly rare, occurring with probability 0.01% per two-qubit gate.

Mitigating and containing leakage errors is an active field of research in superconducting quantum processors in general
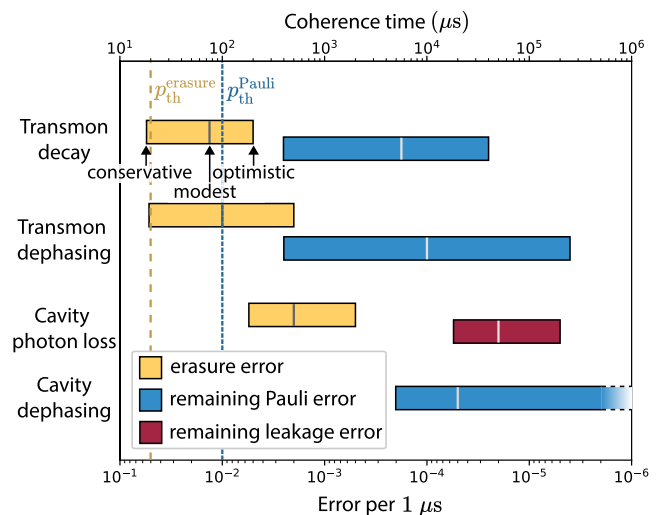

Fig. 5. Error hierarchy in the dual-rail encoding with superconducting cavities during operations. This is a visualization of the most important errors presented in Table 2. The most likely errors in the system are energy relaxation and pure dephasing in the ancilla transmon, followed by single-photon loss in the cavities. All of these errors can be converted into erasure errors to first order (yellow), leaving a significantly smaller, second-order floor of residual Pauli errors (blue) and leakage errors (dark red). The remaining first-order Pauli error is pure dephasing in the cavities, which is intrinsically low in superconducting cavities, especially when compared to all other error rates. For all physical error types, we give a range for the error probability per 1 μs based on error rates typically found in the literature, from conservative (high error rate) to optimistic (low error rate). The values discussed in the main text are based on modest expectations for all components indicated by the colored lines. Remaining Pauli errors due to the transmons are estimated by squaring the transmon error rates, and we assume a 99% conversion efficiency for detecting single-photon loss, expected mainly due to transmon dephasing during joint-parity measurements. We also highlight the approximate thresholds for erasure and Pauli errors in a surface code architecture, $p_{\text{th}}^{\text{erasure}} = 5\%$ and $p_{\text{th}}^{\text{Pauli}} = 1\%$, respectively, with vertical dashed lines, demonstrating that today's modest hardware is already expected to be well below threshold using our proposed dual-rail encoding.

(61, 113). Even with finite erasure conversion efficiency, missed photon loss errors into the ground state are still detected with high probability in later rounds of erasure conversion, meaning a constant, small fraction ($\sim 10^{-5}$ in equilibrium if we assume 10^{-3} probability of leakage and 99% erasure conversion efficiency) of dual-rail qubits remain in $|00\rangle$. Attempts to perform entangling gates with a qubit in $|00\rangle$ result in an identity operation instead. At worst, these leaked states act as a source of Pauli errors on surrounding unleaked qubits whenever we attempt an entangling gate, until they are eventually detected and reset by reinitialization into the dual-rail subspace. Importantly, the fraction of leaked qubits is not expected to grow in time. All other forms of leakage are expected to be extremely rare but in principle can also be detected with the appropriate transmon measurements.

These properties make dual-rail qubits immediately desirable for general quantum computing applications. For NISQ-era algorithms (14), we can run short-depth circuits with postselection, abandoning a circuit run if any erasures are detected, resulting in very low SPAM errors and high effective gate fidelity. The yield of successful circuit attempts decreases exponentially with circuit depth, but for the runs we keep, only very low Pauli error probabilities will remain. With 1% erasure probability, we expect to run circuits with up to ~ 100 two-qubit gates before the success probability becomes impractically low. We emphasize that dual-rail qubit Pauli errors scale quadratically with ancilla transmon lifetimes when operating the transmon in the g-f-manifold, whereas Pauli errors in a transmon-only architecture scale linearly. Thus, we expect dual-rail qubit gate fidelities to improve faster than transmon qubit gate fidelities as transmon coherences continue to improve, while the transmon remains the dominant error source.

B. Scalability. Perhaps the most exciting use of dual-rail cavity qubits is as the "physical qubits" used to encode the logical qubits of a topological fault-tolerant error-correcting code such as the surface code. Many QEC codes can tolerate erasure errors much better than Pauli errors (50), which is reflected in their respective error thresholds (53, 54, 114). While the exact threshold is highly dependent on the order of gate operations and frequency of error detection, for simplicity, we envision performing error detection (via joint-parity measurements) after every two-qubit $ZZ(\theta)$ gate. A general version of this noise model was previously studied for a neutral atoms platform (66), where the threshold for erasure errors was about 5 times higher than for Pauli errors, even with finite detection efficiency. However, error detection after every two-qubit gate may not be the best strategy for the dual-rail encoding but will likely depend on the hardware parameters and relative cost of performing error detection.

We are also aware of the seemingly higher erasure thresholds that exist in measurement-based error correction schemes (53). However, the obtained thresholds highly depend on the underlying error model and are actually similar to gate-based approaches under more realistic scenarios (115). In general, a fair comparison with gate-based approaches based on only the thresholds requires detailed accounting of the number of steps needed to prepare and measure the resource states, as well as detailed knowledge of circuit-level noise, and is therefore beyond the scope of this manuscript. Undoubtedly, a measurement-based approach requires more physical qubits, an overhead which could otherwise be used to increase the code distance or number of logical qubits in a gate-based approach.

Since a surface code of distance d can tolerate up to $d - 1$ erasure errors per error correction cycle but only $(d - 1)/2$ Pauli

errors, erasure errors not only have higher thresholds but scale better with increasing code distance. To put this into perspective, for a fixed distance $d = 11$, a surface code with only erasure errors at $\sim 1\%$ per two-qubit gate will have roughly the same performance as the same surface code with only Pauli errors at $\sim 0.05\%$ per gate, resulting in logical error rates $\sim 10^{-8}$ per cycle. In general, when both Pauli and erasures are present, we need to ensure that both error rates are substantially below their thresholds (66).

Despite tremendous efforts in realizing transmon-based surface codes, reaching physical error rates far below the Pauli threshold is still a major outstanding challenge (15, 62, 116). We believe our approach offers a compelling alternative, whereby error detection opens a shortcut to achieving error rates far

Possible surface code implementation

Legend:

 = Cavity in a dual-rail data qubit

 = Cavity in a dual-rail ancilla qubit
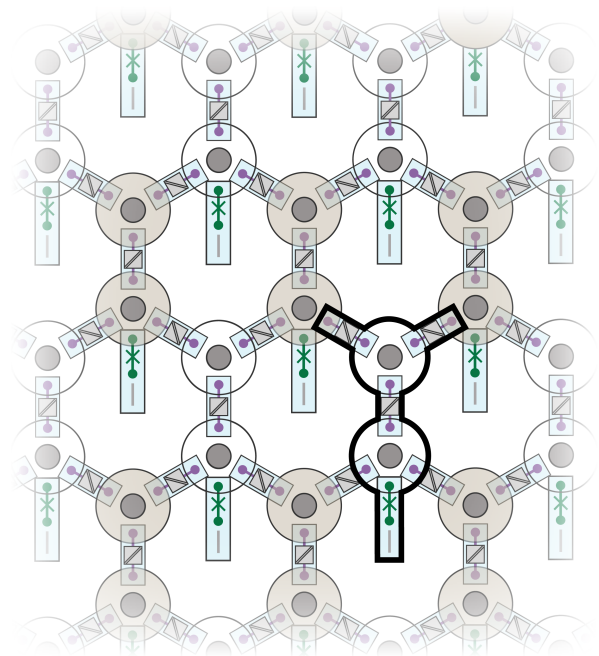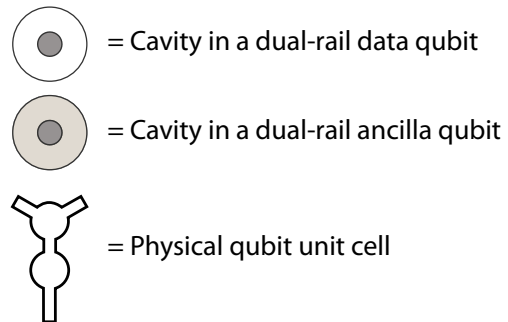
 = Physical qubit unit cell

Fig. 6. Dual-rail cavity qubits forming the physical qubits in a lattice-based quantum error correction code. A single unit cell in the bulk of the lattice is outlined in black and composed of two superconducting cavities (circles), a single ancilla transmon (green) with readout (gray), and three beamsplitter couplers (purple). Within a surface code, the nominally identical dual-rail qubits may play the role of either data qubits (white cavities), which store the quantum information, or measurement qubits (gray cavities), which are used to perform stabilizer measurements during rounds of error correction. Nearest-neighbor connectivity between cavities is sufficient to build a 2D square lattice of dual-rail physical qubits since entangling gates only require one cavity from each dual-rail qubit to interact together (Fig. 4).

below the relevant thresholds, without the need to drastically increase coherence times.

The favorable scaling of erasure errors with distance indicates that detecting first-order hardware errors and flagging them as erasures is almost as good as fully correcting them at the hardware level. Both approaches scale the same with code distance, d, and differ only by a prefactor that characterizes the respective overheads. Rather than correcting quantum errors at the hardware level, we now error detect at the hardware level and reset the erased qubits, a simpler task overall.

Finally, scaling up with a 3D cavity dual-rail architecture has the potential to greatly suppress unwanted cross-talk and package modes in a multiqubit processor as well as correlated errors between the physical qubits. A conceptual illustration of a 2D square lattice of dual-rail qubits required to implement a topological quantum error correction code is shown in Fig. 6. The fact that we can interact with a dual-rail qubit through either one of the cavities means we can reduce the co-ordination number for each cavity mode in lattice-based QEC codes, while maintaining nearest-neighbor connectivity among the dual-rail qubits. The unit cell of our lattice consists of a dual-rail qubit, comprising two superconducting cavity modes, a transmon with readout and a switchable beamsplitter coupler between the cavity modes, and two additional beamsplitter couplers to interface with neighboring unit cells. In comparison, a transmon-based surface code may have unit cells consisting of a single transmon and two coupling elements.

In general, increasing the code distance of a surface code exponentially suppresses the logical error rate, provided physical error rates remain well below threshold when increasing the number of hardware components. Alternatively, one can focus on reducing the physical error rate further below threshold, which gives a similar exponential improvement. In the dual-rail encoding, we are willing to increase the complexity of our physical qubit in return for significantly lower physical error rates, which now also reduce quadratically with improvements in transmon coherence times (88). When we then scale up to larger code distances, this likely results in far fewer hardware components to reach a target logical error rate and allows an additional margin for sources of errors associated with scaling up any qubit architecture.

3. Conclusion

We have introduced the dual-rail cavity qubit for circuit-QED, which leverages the intrinsic noise bias of microwave cavities and the dual-rail code to make a fully error-detected logical qubit. In this paradigm, we now detect and convert the dominant first-order hardware errors to erasure errors, leaving a small undetected background of second-order errors which become Pauli errors. We expect erasures per gate at the $\sim 1\%$ level and Pauli errors at the $\sim 0.01\%$ level for typical present-day coherence times, making both values well below their respective thresholds of $\sim 5\%$ and $\sim 1\%$, respectively. Furthermore, all leakage out of the logical subspace can in principle be detected. Most importantly, this strong hierarchy of errors can be maintained while performing single and two-qubit gates, thereby relaxing the requirements for

quantum error correction, and the realization of a fault-tolerant quantum computer. Each dual-rail qubit can play the role of a physical qubit in a surface code, where erasures are significantly easier to correct than Pauli errors, having both a higher threshold and superior scaling with code distance.

Our results suggest that the dual-rail code is the most efficient bosonic encoding for microwave cavities, benefiting greatly from straightforward single-qubit gates, measurement, and state preparation while incurring minimal photon number overhead relative to other bosonic codes. Realizing all logical operations is imminently achievable, with all hardware requirements already demonstrated. With today's typical coherence times, we anticipate being significantly below the effective threshold for a surface code with erasure and Pauli errors present. Since this approach makes all physical errors second-order at the hardware level, we also predict that the performance of dual-rail qubits will improve more rapidly than conventional schemes as coherence times improve further. Finally, this paradigm can find immediate use in implementing near-term short-depth circuits with postselection to improve the utility of today's NISQ applications.

4. Materials and Methods

For the simulation results in Fig. 2, we model transmon readout by considering two dominant sources of readout error. This is decay of the transmon during the readout pulse and the finite separation of the transmon's pointer states with the full error model detailed in *SI Appendix*, Section A. Further details on how Lindblad master equation simulations were used to model the entire logical readout protocol can be found in *SI Appendix*, Section B. We can also adjust the measurement decoding scheme to either favor low erasure rates or low logical assignment errors.

Author affiliations: [a]Department of Applied Physics, Yale University, New Haven, CT 06511; [b]Department of Physics, Yale University, New Haven, CT 06511; and [c]Yale Quantum Institute, Yale University, New Haven, CT 06511

Author contributions: J.D.T., P.W., J.C., T.T., L.F., S.M.G., S.P., and R.J.S. designed research; J.D.T., P.W., H.K.B., B.J.C., S.J.d.G., J.W.O.G., W.D.K., Y.L., A.M., K.S., N.T., and S.H.X. performed research; J.D.T., P.W., B.J.C., S.J.d.G., J.W.O.G., Y.L., A.M., and S.H.X. analyzed data; J.D.T. performed simulations and proposed the concept; P.W., H.K.B., W.D.K., K.S., and N.T. performed simulations; R.J.S. supervised the project; and J.D.T., P.W., and R.J.S. wrote the paper.

1. J. I. Cirac, P. Zoller, Quantum computations with cold trapped ions. *Phys. Rev. Lett.* **74**, 4091–4094 (1995).
2. T. Monz *et al.*, 14-qubit entanglement: Creation and coherence. *Phys. Rev. Lett.* **106**, 130506 (2011).
3. D. Leibfried, R. Blatt, C. Monroe, D. Wineland, Quantum dynamics of single trapped ions. *Rev. Mod. Phys.* **75**, 281–324 (2003).
4. R. Blatt, C. F. Roos, Quantum simulations with trapped ions. *Nat. Phys.* **8**, 277–284 (2012).

5. H. Häffner, C. Roos, R. Blatt, Quantum computing with trapped ions. *Phys. Rep.* **469**, 155–203 (2008).
6. I. Bloch, J. Dalibard, W. Zwerger, Many-body physics with ultracold gases. *Rev. Mod. Phys.* **80**, 885–964 (2008).
7. M. Saffman, T. G. Walker, K. Mølmer, Quantum information with Rydberg atoms. *Rev. Mod. Phys.* **82**, 2313–2363 (2010).
8. I. Bloch, J. Dalibard, S. Nascimbène, Quantum simulations with ultracold quantum gases. *Nat. Phys.* **8**, 267–276 (2012).
9. M. Saffman, Quantum computing with atomic qubits and Rydberg interactions: Progress and challenges. *J. Phys. B: At. Mol. Opt. Phys.* **49**, 202001 (2016).
10. A. Wallraff *et al.*, Strong coupling of a single photon to a superconducting qubit using circuit quantum electrodynamics. *Nature* **431**, 162–167 (2004).
11. A. Blais, R. S. Huang, A. Wallraff, S. M. Girvin, R. J. Schoelkopf, Cavity quantum electrodynamics for superconducting electrical circuits: An architecture for quantum computation. *Phys. Rev. A* **69**, 062320 (2004).
12. F. Arute *et al.*, Quantum supremacy using a programmable superconducting processor. *Nature* **574**, 505–510 (2019).
13. S. Xu, *et al.* Digital simulation of non-abelian anyons with 68 programmable superconducting qubits. arXiv [Preprint] (2022). http://arxiv.org/abs/2211.09802 (Accessed 17 July 2023).
14. J. Preskill, Quantum computing in the NISQ era and beyond. *Quantum* **2**, 79 (2018).
15. R. Acharya *et al.*, Suppressing quantum errors by scaling a surface code logical qubit. *Nature* **614**, 676–681 (2023).
16. R. Gallager, Low-density parity-check codes. *IRE Trans. Inf. Theory* **8**, 21–28 (1962).
17. M. Mirrahimi *et al.*, Dynamically protected cat-qubits: A new paradigm for universal quantum computation. *New J. Phys.* **16**, 045014 (2014).
18. S. Puri *et al.*, Stabilized cat in a driven nonlinear cavity: A fault-tolerant error syndrome detector. *Phys. Rev. X* **9**, 041009 (2019).
19. A. Grimm *et al.*, Stabilization and operation of a Kerr-cat qubit. *Nature* **584**, 205–209 (2020).
20. J. Venkatraman, R. G. Cortinas, N. E. Frattini, X. Xiao, M. H. Devoret, Quantum interference of tunneling paths under a double-well barrier. arXiv [Preprint] (2022). http://arxiv.org/abs/2211.04605 (Accessed 17 July 2023).
21. N. E. Frattini *et al.* The squeezed Kerr oscillator: Spectral kissing and phase-flip robustness. arXiv [Preprint] (2022). http://arxiv.org/abs/2209.03934 (Accessed 17 July 2023).
22. J. Chavez-Carlos *et al.*, Spectral kissing and its dynamical consequences in the squeezed Kerr-nonlinear oscillator. arXiv [Preprint] (2022). http://arxiv.org/abs/2210.07255 (Accessed 17 July 2023).
23. I. Cong *et al.*, Hardware-efficient, fault-tolerant quantum computation with Rydberg atoms. *Phys. Rev. X* **12**, 021049 (2022).
24. P. Aliferis, J. Preskill, Fault-tolerant quantum computation against biased noise. *Phys. Rev. A* **78**, 052331 (2008).
25. J. P. Bonilla Ataides, D. K. Tuckett, S. D. Bartlett, S. T. Flammia, B. J. Brown, The xzzx surface code. *Nat. Commun.* **12**, 2172 (2021).
26. A. S. Darmawan, B. J. Brown, A. L. Grimsmo, D. K. Tuckett, S. Puri, Practical quantum error correction with the xzzx code and Kerr-cat qubits. *PRX Quant.* **2**, 030345 (2021).
27. C. Chamberland *et al.*, Building a fault-tolerant quantum computer using concatenated cat codes. *PRX Quant.* **3**, 010329 (2022).
28. J. Guillaud, M. Mirrahimi, Repetition cat qubits for fault-tolerant quantum computation. *Phys. Rev. X* **9**, 041053 (2019).
29. A. Kubica, A. Haim, Y. Vaknin, F. Brandao, A. Retzker, Erasure qubits: Overcoming the t_1 limit in superconducting circuits. arXiv [Preprint] (2022). http://arxiv.org/abs/2208.05461 (Accessed 17 July 2023).
30. J. Roffe, L. Z. Cohen, A. O. Quintavalle, D. Chandra, E. T. Campbell, Bias-tailored quantum LDPC codes. arXiv [Preprint] (2022). http://arxiv.org/abs/2202.01702 (Accessed 17 July 2023).
31. T. J. Yoder, R. Takagi, I. L. Chuang, Universal fault-tolerant gates on concatenated stabilizer codes. *Phys. Rev. X* **6**, 031039 (2016).
32. C. Lin, G. Yang, X. Song, M. A. Perkowski, X. Li, An universal quantum computation scheme with low error diffusion property. arXiv [Preprint] (2023). http://arxiv.org/abs/2105.07133 (Accessed 17 July 2023).
33. R. Chao, B. W. Reichardt, Quantum error correction with only two extra qubits. *Phys. Rev. Lett.* **121**, 050502 (2018).
34. L. Postler *et al.*, Demonstration of fault-tolerant universal quantum gate operations. *Nature* **605**, 675–680 (2022).
35. P. Gokhale *et al.*, "Asymptotic improvements to quantum circuits via qutrits" in *Proceedings of the 46th International Symposium on Computer Architecture, ISCA '19* (Association for Computing Machinery, New York, NY, 2019), pp. 554–566.
36. W. Cai, Y. Ma, W. Wang, C. L. Zou, L. Sun, Bosonic quantum error correction codes in superconducting quantum circuits. *Fundam. Res.* **1**, 50–67 (2021).
37. D. Gottesman, A. Kitaev, J. Preskill, Encoding a qubit in an oscillator. *Phys. Rev. A* **64**, 012310 (2001).
38. C. Flühmann *et al.*, Encoding a qubit in a trapped-ion mechanical oscillator. *Nature* **566**, 513–517 (2019).
39. P. Campagne-Ibarcq *et al.*, Quantum error correction of a qubit encoded in grid states of an oscillator. *Nature* **584**, 368–372 (2020).
40. V. V. Sivak *et al.*, Real-time quantum error correction beyond break-even. *Nature* **616**, 50–55 (2023).
41. A. L. Grimsmo, S. Puri, Quantum error correction with the Gottesman–Kitaev-preskill code. *PRX Quant.* **2**, 020101 (2021).
42. S. Haroche, J. M. Raimond, *Exploring the Quantum: Atoms, Cavities, and Photons* (Oxford University Press, 2006).
43. B. Vlastakis *et al.*, Deterministically encoding quantum information using 100-photon schrödinger cat states. *Science* **342**, 607–610 (2013).
44. Z. Leghtas *et al.*, Confining the state of light to a quantum manifold by engineered two-photon loss. *Science* **347**, 853–857 (2015).
45. N. Ofek *et al.*, Extending the lifetime of a quantum bit with error correction in superconducting circuits. *Nature* **536**, 441–445 (2016).
46. M. H. Michael *et al.*, New class of quantum error-correcting codes for a bosonic mode. *Phys. Rev. X* **6**, 031006 (2016).
47. L. Hu *et al.*, Quantum error correction and universal gate set operation on a binomial bosonic logical qubit. *Nat. Phys.* **15**, 503–508 (2019).
48. Y. Xu *et al.*, Demonstration of controlled-phase gates between two error-correctable photonic qubits. *Phys. Rev. Lett.* **124**, 120501 (2020).
49. Z. Ni *et al.*, Beating the break-even point with a discrete-variable-encoded logical qubit. *Nature* **616**, 56–60 (2023).
50. M. Grassl, T. Beth, T. Pellizzari, Codes for the quantum erasure channel. *Phys. Rev. A* **56**, 33–38 (1997).
51. D. Gottesman, "Stabilizer codes and quantum error correction," PhD thesis, California Institute of Technology, Pasadena, CA (1997).
52. T. M. Stace, S. D. Barrett, A. C. Doherty, Thresholds for topological codes in the presence of loss. *Phys. Rev. Lett.* **102**, 200501 (2009).
53. S. D. Barrett, T. M. Stace, Fault tolerant quantum computation with very high threshold for loss errors. *Phys. Rev. Lett.* **105**, 200502 (2010).
54. N. Delfosse, G. Zémor, Linear-time maximum likelihood decoding of surface codes over the quantum erasure channel. *Phys. Rev. Res.* **2**, 033042 (2020).
55. P. Aliferis *et al.*, Fault-tolerant computing with biased-noise superconducting qubits: A case study. *New J. Phys.* **11**, 013061 (2009).
56. A. G. Fowler, Coping with qubit leakage in topological codes. *Phys. Rev. A* **88**, 042308 (2013).
57. J. Ghosh, A. G. Fowler, Leakage-resilient approach to fault-tolerant quantum computing with superconducting elements. *Phys. Rev. A* **91**, 020302 (2015).
58. M. Suchara, A. W. Cross, J. M. Gambetta, "Leakage suppression in the toric code" in *2015 IEEE International Symposium on Information Theory (ISIT)* (2015), pp. 1119–1123.
59. C. C. Bultink *et al.*, Protecting quantum entanglement from leakage and qubit errors via repetitive parity measurements. *Sci. Adv.* **6**, eaay3050 (2020).
60. B. M. Varbanov *et al.*, Leakage detection for a transmon-based surface code. *npj Quant. Inf.* **6**, 102 (2020).
61. M. McEwen *et al.*, Removing leakage-induced correlated errors in superconducting quantum error correction. *Nat. Commun.* **12**, 1761 (2021).
62. S. Krinner *et al.*, Realizing repeated quantum error correction in a distance-three surface code. *Nature* **605**, 669–674 (2022).
63. Y. Li, P. C. Humphreys, G. J. Mendoza, S. C. Benjamin, Resource costs for fault-tolerant linear optical quantum computing. *Phys. Rev. X* **5**, 041007 (2015).
64. T. Rudolph, Why i am optimistic about the silicon-photonic route to quantum computing. *APL Photonics* **2**, 030901 (2017).
65. S. Bartolucci *et al.*, Fusion-based quantum computation. *Nat. Commun.* **14**, 912 (2023).
66. Y. Wu, S. Kolkowitz, S. Puri, J. D. Thompson, Erasure conversion for fault-tolerant quantum computing in alkaline earth Rydberg atom arrays. *Nat. Commun.* **13**, 4657 (2022).
67. C. Axline *et al.*, An architecture for integrating planar and 3D cQED devices. *Appl. Phys. Lett.* **109**, 042601 (2016).
68. M. Reagor *et al.*, Quantum memory with millisecond coherence in circuit QED. *Phys. Rev. B* **94**, 014506 (2016).
69. A. Romanenko, D. I. Schuster, Understanding quality factor degradation in superconducting niobium cavities at low microwave field amplitudes. *Phys. Rev. Lett.* **119**, 264801 (2017).
70. O. Milul *et al.*, A superconducting quantum memory with tens of milliseconds coherence time. arXiv [Preprint] (2023). http://arxiv.org/abs/2302.06442 (Accessed 17 July 2023).
71. S. Rosenblum *et al.*, Fault-tolerant detection of a quantum error. *Science* **361**, 266–270 (2018).
72. A. Eickbusch *et al.*, Fast universal control of an oscillator with weak dispersive coupling to a qubit. *Nat. Phys.* **18**, 1464–1469 (2022).
73. R. W. Heeres *et al.*, Implementing a universal gate set on a logical qubit encoded in an oscillator. *Nat. Commun.* **8**, 94 (2017).
74. P. Reinhold *et al.*, Error-corrected gates on an encoded qubit. *Nat. Phys.* **16**, 822–826 (2020).
75. L. D. Burkhart *et al.*, Error-detected state transfer and entanglement in a superconducting quantum network. *PRX Quant.* **2**, 030321 (2021).
76. Y. Lu *et al.*, A high-fidelity microwave beamsplitter with a parity-protected converter. arXiv [Preprint] (2023). https://doi.org/10.48550/arXiv.2303.00959 (Accessed 17 July 2023).
77. B. J. Chapman *et al.*, High-on-off-ratio beam-splitter interaction for gates on bosonically encoded qubits. *PRX Quant.* **4**, 020355 (2023).
78. S. B. Bravyi, A. Yu. Kitaev, Quantum codes on a lattice with boundary. arXiv [Preprint] (1998). http://arxiv.org/abs/quant-ph/9811052 (Accessed 17 July 2023).
79. E. Dennis, A. Kitaev, A. Landahl, J. Preskill, Topological quantum memory. *J. Math. Phys.* **43**, 4452–4505 (2002).
80. A. G. Fowler, M. Mariantoni, J. M. Martinis, A. N. Cleland, Surface codes: Towards practical large-scale quantum computation. *Phys. Rev. A* **86**, 032324 (2012).
81. M. Reagor *et al.*, Reaching 10 ms single photon lifetimes for superconducting aluminum cavities. *Appl. Phys. Lett.* **102**, 192604 (2013).
82. I. L. Chuang, Y. Yamamoto, Simple quantum computer. *Phys. Rev. A* **52**, 3489–3496 (1995).
83. H. Levine *et al.*, Demonstrating a long-coherence dual-rail erasure qubit using tunable transmons. arXiv [Preprint] (2023). http://arxiv.org/abs/2307.08737 (Accessed 17 July 2023).
84. E. Zakka-Bajjani *et al.*, Quantum superposition of a single microwave photon in two different 'colour' states. *Nat. Phys.* **7**, 599–603 (2011).
85. Z. Leghtas *et al.*, Hardware-efficient autonomous quantum memory protection. *Phys. Rev. Lett.* **111**, 120501 (2013).
86. J. Bylander *et al.*, Noise spectroscopy through dynamical decoupling with a superconducting flux qubit. *Nat. Phys.* **7**, 565–570 (2011).
87. F. Yan *et al.*, Rotating-frame relaxation as a noise spectrum analyser of a superconducting qubit undergoing driven evolution. *Nat. Commun.* **4**, 2337 (2013).
88. T. Tsunoda *et al.*, Error-detectable bosonic entangling gates with a noisy ancilla. *PRX Quant.* **4**, 020354 (2023).
89. S. S. Elder *et al.*, High-fidelity measurement of qubits encoded in multilevel superconducting circuits. *Phys. Rev. X* **10**, 011001 (2020).
90. L. Sun *et al.*, Tracking photon jumps with repeated quantum non-demolition parity measurements. *Nature* **511**, 444–448 (2014).

91. A. Wallraff *et al.*, Sideband transitions and two-tone spectroscopy of a superconducting qubit strongly coupled to an on-chip cavity. *Phys. Rev. Lett.* **99**, 050501 (2007).
92. S. Premaratne, F. Wellstood, B. Palmer, Microwave photon Fock state generation by stimulated Raman adiabatic passage. *Nat. Commun.* **8**, 14148 (2017).
93. S. Rosenblum *et al.*, A CNOT gate between multiphoton qubits encoded in two cavities. *Nat. Commun.* **9**, 652 (2018).
94. E. Jeffrey *et al.*, Fast accurate state measurement with superconducting qubits. *Phys. Rev. Lett.* **112**, 190504 (2014).
95. T. Walter *et al.*, Rapid high-fidelity single-shot dispersive readout of superconducting qubits. *Phys. Rev. Appl.* **7**, 054020 (2017).
96. D. Egger *et al.*, Pulsed reset protocol for fixed-frequency superconducting qubits. *Phys. Rev. Appl.* **10**, 044030 (2018).
97. Y. Sunada *et al.*, Fast readout and reset of a superconducting qubit coupled to a resonator with an intrinsic purcell filter. *Phys. Rev. Appl.* **17**, 044016 (2022).
98. K. S. Chou *et al.*, Demonstrating a superconducting dual-rail cavity qubit with erasure-detected logical measurements. arXiv [Preprint] (2023). https://doi.org/10.48550/arXiv.2307.03169 (Accessed 17 July 2023).
99. K. R. Brown, A. W. Harrow, I. L. Chuang, Arbitrarily accurate composite pulse sequences. *Phys. Rev. A* **70**, 052318 (2004).
100. W. G. Alway, J. A. Jones, Arbitrary precision composite pulses for NMR quantum computing. *J. Magn. Reson.* **189**, 114–120 (2007).
101. J. M. Chow *et al.*, Optimized driving of superconducting artificial atoms for improved single-qubit gates. *Phys. Rev. A* **82**, 040305 (2010).
102. F. Motzoi, J. M. Gambetta, P. Rebentrost, F. K. Wilhelm, Simple pulses for elimination of leakage in weakly nonlinear qubits. *Phys. Rev. Lett.* **103**, 110501 (2009).
103. J. M. Gambetta, F. Motzoi, S. T. Merkel, F. K. Wilhelm, Analytic control methods for high-fidelity unitary operations in a weakly nonlinear oscillator. *Phys. Rev. A* **83**, 012308 (2011).
104. R. W. Heeres *et al.*, Cavity state manipulation using photon-number selective phase gates. *Phys. Rev. Lett.* **115**, 137002 (2015).
105. C. Wang *et al.*, A Schrodinger cat living in two boxes. *Science* **352**, 1087–1091 (2016).
106. F. Mallet *et al.*, Single-shot qubit readout in circuit quantum electrodynamics. *Nat. Phys.* **5**, 791–795 (2009).
107. Z. Chen *et al.*, Measuring and suppressing quantum state leakage in a superconducting qubit. *Phys. Rev. Lett.* **116**, 020501 (2016).
108. P. Magnard *et al.*, Fast and unconditional all-microwave reset of a superconducting qubit. *Phys. Rev. Lett.* **121**, 060502 (2018).
109. P. Campagne-Ibarcq *et al.*, Persistent control of a superconducting qubit by stroboscopic measurement feedback. *Phys. Rev. X* **3**, 021008 (2013).
110. W. L. Ma *et al.*, Path-independent quantum gates with noisy ancilla. *Phys. Rev. Lett.* **125**, 110503 (2020).
111. Y. Makhlin, Nonlocal properties of two-qubit gates and mixed states, and the optimization of quantum computations. *Quant. Inf. Process.* **1**, 243–252 (2002).
112. N. Schuch, J. Siewert, Natural two-qubit gate for quantum computation using the *XY* interaction. *Phys. Rev. A* **67**, 032301 (2003).
113. K. C. Miao *et al.*, Overcoming leakage in scalable quantum error correction. arXiv [Preprint] (2022). http://arxiv.org/abs/2211.04728 (Accessed 17 July 2023).
114. D. S. Wang, A. G. Fowler, L. C. L. Hollenberg, Surface code quantum computing with error rates over 1%. *Phys. Rev. A* **83**, 020302 (2011).
115. A. C. Whiteside, A. G. Fowler, Upper bound for loss in practical topological-cluster-state quantum computing. *Phys. Rev. A* **90**, 052316 (2014).
116. J. F. Marques *et al.*, Logical-qubit operations in an error-detecting surface code. *Nat. Phys.* **18**, 80–86 (2022).
117. Y. Y. Gao *et al.*, Entanglement of bosonic modes through an engineered exchange interaction. *Nature* **566**, 509–512 (2019).
118. A. Morvan *et al.*, Qutrit randomized benchmarking. *Phys. Rev. Lett.* **126**, 210504 (2021).
119. J. Koch *et al.*, Charge-insensitive qubit design derived from the Cooper pair box. *Phys. Rev. A* **76**, 042319 (2007).
120. M. J. Peterer, Coherence and decay of higher energy levels of a superconducting transmon qubit. *Phys. Rev. Lett.* **114**, 010501 (2015).
121. E. Knill, R. Laflamme, G. J. Milburn, A scheme for efficient quantum computation with linear optics. *Nature* **409**, 46 (2001).
122. R. Bianchetti *et al.*, Control and tomography of a three level superconducting artificial atom. *Phys. Rev. Lett.* **105**, 223601 (2010).
123. D. Ristè, J. G. van Leeuwen, H.-S. Ku, K. W. Lehnert, L. DiCarlo, Initialization by measurement of a superconducting quantum bit circuit. *Phys. Rev. Lett.* **109**, 050507 (2012).
124. J. Teoh, Dual rail logical measurement simulation code. Github. https://github.com/james-teoh/PNASDualRailPaperCode2023. Deposited 22 September 2023.